

Optical Optimization of A Multi-Slit Extreme Ultraviolet Spectrograph for Global Solar Corona Diagnostics

Yufei Feng^{1,2}, Xianyong Bai^{1,2,3,4*}, Sifan Guo^{1,3}, Hui Tian⁵,
Lami Chan⁵, Yuanyong Deng^{1,2,3}, Qi Yang^{1,3}, Wei Duan^{1,2,3},
Xiaoming Zhu^{1,2}, Xiao Yang^{1,2,3}, Zhiwei Feng^{1,2,3},
Zhiyong Zhang^{1,2,3}

^{1*}National Astronomical Observatories, Chinese Academy of Sciences,
Beijing, 1001101, China.

²Key Laboratory of Solar Activity and Space Weather, National Space
Science Center, Chinese Academy of Sciences, Beijing, 100190, China.

³School of Astronomy and Space Sciences, University of Chinese
Academy of Sciences, Beijing, 100049, China.

⁴Institute for Frontiers in Astronomy and Astrophysics, Beijing Normal
University, Beijing, 102206, China.

⁵School of Earth and Space Sciences, Peking University, Beijing, 100871,
China.

*Corresponding author(s). E-mail(s): xybai@bao.ac.cn;

Abstract

The spatial-temporal evolution of coronal plasma parameters of the solar outer atmosphere at global scales, derived from solar full-disk imaging spectroscopic observation in the extreme-ultraviolet band, is critical for understanding and forecasting solar eruptions. We propose a multi-slits extreme ultraviolet imaging spectrograph for global coronal diagnostics with high cadence and present the preliminary instrument designs for the wavelength range from 18.3 to 19.8 nm. The instrument takes a comprehensive approach to obtain global coronal spatial and spectral information, improve the detected cadence and avoid overlapping. We first describe the relationship between optical properties and structural parameters, especially the relationship between the overlapping and the number of slits, and give a general multi-slits extreme-ultraviolet imaging spectrograph design process. The multilayer structure is optimized to enhance the effective areas in

the observation band. Five distantly-separated slits are set to divide the entire solar field of view, which increase the cadence for raster scanning the solar disk by 5 times relative to a single slit. The spectral resolving power of the optical system with an aperture diameter of 150 mm are optimized to be greater than 1461. The spatial resolution along the slits direction and the scanning direction are about $4.4''$ and $6.86''$, respectively. The Al/Mo/B₄C multilayer structure is optimized and the peak effective area is about 1.60 cm² at 19.3 nm with a full width at half maximum of about 1.3 nm. The cadence to finish full-disk raster scan is about 5 minutes. Finally, the instrument performance is evaluated by an end-to-end calculation of the system photon budget and a simulation of the observational image and spectra. Our investigation shows that this approach is promising for global coronal plasma diagnostics.

Keywords: Sun, Corona, Extreme ultraviolet imaging spectroscopy, Full-disk

1 Introduction

Coronal mass ejections (CMEs) and flares are two of the most violent phenomena in the solar system that can cause disastrous space weather events. Up to now, the physical mechanisms that initiate and drive CMEs and flares, are not fully understood. Currently, it is widely accepted that they are mainly generated in the corona, i.e., the outermost layer of the solar atmosphere. Obtaining global maps of coronal plasma parameters including density, velocity and line width, with a high cadence will significantly improve our understanding of CMEs and flares (e.g., [Tian et al, 2021](#); [Del Zanna and Mason, 2018](#); [Young, 2021](#)). In addition, such global maps are important for identifying the source regions of solar wind (e.g., [Tian et al, 2021](#); [Brooks et al, 2015](#)), which provides critical constraints for heliospheric models.

Extreme ultraviolet (EUV) spectroscopic observations provide a way to realize rapid and accurate measurements of global distributions of coronal plasma parameters. [Ugarte-Urra et al, 2023](#) claimed that a EUV instrument providing consistent full-disk sampling of plasma properties at the dynamic timescales of solar eruptive phenomena will revolutionize the field by adding the spectral diagnostics. The following parameters should be considered for such instruments: **(1)** full-disk field of view (FOV) to monitor the global distributions of various coronal features such as active region (AR) loops, coronal holes (CHs), flare, CMEs and filaments, etc.; **(2)** moderate spatial resolution of about 6 arcseconds or better to resolve EUV bright points, coronal plumes, and AR loops; **(3)** cadence of several minutes to capture the evolution of the CMEs and flares; **(4)** covering a narrow spectral band that contains a series of strong coronal lines for diagnosing density and velocity. In other words, an EUV imaging spectrograph that has the ability to rapidly obtain coronal imaging and spectral information with a full-disk FOV is needed.

At present, there are four main types of EUV spectrographs used to capture coronal imaging and spectral information.

The first one is a single-slit imaging spectroscopy, for example, the Solar Ultraviolet Measurements of Emitted Radiation (SUMER) onboard the Solar and Heliospheric

Observatory (SOHO) launched in 1995 (Wilhelm et al, 1995; Domingo et al, 1995), the EUV Imaging Spectrograph (EIS) onboard the Hinode mission in 2006 (Culhane et al, 2007; Mariska et al, 2007; Korendyke et al, 2006) and the Spectral Imaging of the Coronal Environment (SPICE) of the Solar Orbiter mission in 2020 (SPICE Consortium et al, 2020). The solar EUV image is focused by the primary mirror, and partially selected through the slit, dispersed by the grating, and the spectrum of slit is recorded at different positions of the detector depending on the wavelength. Finally, two-dimensional images and spectral information are obtained by scanning the primary mirror step by step. It takes hours to sample a region with a typical size of an active region in this manner, greatly limiting the investigation of the evolution of dynamic events at global scales. In addition, there is a specialized version, exemplified by the Rapid Acquisition Imaging Spectrograph Experiment (RAISE) conducted by the United States Sounding Rocket in 2016 (Laurent et al, 2016). For the strong radiation lines (Ly α at 121.6 nm), the instrument can observe small-scale multithermal dynamics in AR and the quiet-Sun (QS) loops with its 3 s raster cadence. But the method is not suitable for weaker target lines as the exposure time will be much longer, and scanning the whole solar disk still takes a few hours.

The second type is a slitless imaging spectroscopy, such as the S082A payload on *Skylab* in the 1970s (Tousey et al, 1977), the Multi-Order Solar EUV Spectrograph (MOSES) on a sounding rocket experiment in 2006 (Fox, 2011), the slitless spectrograph of the COronal Spectroscopic Imager in the EUV (COSIE-S) proposed in 2019 (Winebarger et al, 2019; Golub et al, 2020) and the slitless spectrograph of The EUV CME and Coronal Connectivity Observatory (ECCCO-S) approved by NASA in 2023 (Reeves et al, 2022). The system consists of only one concave grating and detector, simultaneously recording the 0^{th} order broadband image and the mixed spectral image after $\pm 1^{st}$ order dispersion (while COSIE records only the spectra of the 2^{nd} order of the blazed grating). This kind of instrument has a high cadence, but there is serious overlap from solar images of adjacent spectral lines, increased difficulty in the inversion of corona physical parameters. In addition, the slot detection of EIS instrument, which obtain solar images of large areas in bright solar emission lines with a single exposure, is more like a detected mode of slitless spectrograph.

The third type is the multi-slit imaging spectroscopy, for example, the Multi-slit Solar Explorer (MUSE), a MIDEEX mission approved by NASA in 2019 (De Pontieu et al, 2020, 2022; Cheung et al, 2022). This approach can be considered as an upgraded version of the first type, featuring multiple closely-separated parallel slits instead of a single slit. Each slit selects a slice on the solar disk. Therefore, the cadence for scanning the same region is reduced several times compared to single-slit imaging spectroscopy. MUSE does not cover a full-disk FOV, as it focused on high spatial resolution (about $0.4''$) observation with a FOV of $170'' \times 170''$.

In addition, a new type of EUV integral field spectrograph (IFS) based on image slicers has emerged, for example, the Spectral Imaging of the Solar Atmosphere (SISA) proposed for the SPARK mission concept (Calcines Rosario et al, 2023). The image slicer, which is the most crucial component of the system, divides the solar disk into numerous small field units. It then transmits them to different gratings, allowing for the capture of both imaging and spectral information simultaneously on the detector. The

image-slicer-based IFS has also been proposed for spectroscopic observations of solar flares at other wavelengths, including the Lyman Alpha Solar Spicule Observatory (LASSO) for the band of 1205.0 Å–1220.0 Å (Chamberlin and Gong, 2016). Additionally, a Integral Field Unit (IFU) based on image slicers has successfully employed in the GREGOR Infrared Spectrograph on the GREGOR Solar Telescope (Dominguez-Tagle et al, 2022). A machined image slicer integral field unit (MISI) is also being developed for the Diffraction-Limited near-IR Spectropolarimeter (DL-NIRSP) of the Daniel K. Inouye Solar Telescope (DKIST) (Lin et al, 2022; Sukegawa et al, 2023; Anan et al, 2024). But the manufacturing technology of image slicers for the EUV are currently under development at Technology Readiness Level (TRL) 4. Hence it needs a long time to realize the EUV solar observation with IFS.

Obviously, none of the exiting and proposed instrument could adequately address all the detection requirements for solar full-disk spectral diagnostics, particularly the need for a combination of a large FOV, negligible spectral overlapping and high cadence.

In this paper we present the preliminary design of a new extreme-ultraviolet imaging spectrograph for global coronal diagnostics with high cadence. Several distantly-separated slits, dividing the full-disk FOV into multiple parts, are designed to carry out the raster scan of the whole solar disk within five minutes. In Section 2, we describe the requirements and principle of the instrument. Optical system design and optimization of effective area are presented in Section 3. The theoretical performance of the proposed instrument is evaluated in Section 4. Finally, we summarize our results in Section 5.

2 Main Instrumental Parameters

Taking full-disk solar spectral diagnostics at EUV wavelength would: (1) monitor and improve our understanding of highly dynamic solar eruption, e.g., flares and CMEs; (2) derive both of the line-of-sight and plane-of-the-sky velocity of CMEs to better investigating the propagation of CMEs in the interplanetary space and forecasting the arrival time of CME at the earth; (3) identify the source regions of solar wind. Chan et al, 2024 described the preliminary consideration for the key instrument parameters. Here we summarize the main results and use them as the input for the instrument design. A field of view of $40' \times 50'$ obtained by rastering 200 steps of $3''$ with 5 slits is helpful for monitoring solar activities in the corona. The spectral range of 18.3–19.8 nm is required to measure coronal electron densities (Fe XII 195.12/186.89 Å) and temperatures (Fe VIII, Fe X, Fe XI, Fe XII) and to investigate the relationship between the evolution of these parameters and solar eruptions. A spatial resolution better than $6''$ is required to resolve EUV bright points, coronal plumes, and AR loops. Spectral resolving power, i.e., the central wavelength λ_0 divided by the half-height full width $\Delta\lambda_0$, must be greater than 500 to resolve the main diagnostic lines and measure the line-of-sight velocity of a CME (Xu et al, 2022; Yang et al, 2022; Lu et al, 2023). A temporal resolution of less than 5 minutes is required for global corona detection to capture the dynamics of CME. The tentatively chosen specifications for the instrument are presented in Table 1.

Table 1 Main parameters for the instrument

Characteristic	Performance Requirement
Raster FOV Φ / \prime	$40' \times 50'$ in 200 raster steps of $3''$ with 5 slits
Temperature ranges/ (log T/K)	5.65–6.20
Spectral range $\Delta\lambda / \text{nm}$	18.3–19.8 (at the center wavelength of 19 nm)
Characteristic spectral line	Fe VIII 185.21 Å, Fe X 184.54 Å, Fe XII 188.22 Å, Fe XII 186.89 Å, Fe XII 193.51 Å and Fe XII 195.12 Å
Spatial resolution/ \prime	~ 6
Spectral resolving power $\lambda_0 / \Delta\lambda_0$	>500 ($\lambda_0 = 19 \text{ nm}$)
Temporal resolution/ s	≤ 300

We use a multi-slits grating spectrograph to achieve the above detection. The whole solar disk can be divided into n regions in the y direction, as shown in Figure 1, and n distantly separated slits are then designated for each region individually. At a certain time t_i , slits are spaced apart in the y_n position, each of which allows a slice of the solar image to pass through with a FOV dy . Multiple slices are dispersed and reimaged, and light of different wavelengths is recorded at different positions on the detector. Therefore, a single exposure can simultaneously obtain spatial information (along the slit) and spectral information (perpendicular to the slit) in multiple slits. At the next time t_{i+1} , the focused solar image is scanned (i.e., rotating the primary mirror) on the multi-slit to the next position $y_n + \delta y$ depended on the scanning step. By scanning step by step, the spatial and spectral information of the entire Sun is recorded sequentially. Finally, we can obtain the global coronal spatial structure as well as spectral information by reconstructing multiple image slices. In fact, the instrument has to take a comprehensive approach to obtain global coronal spatial and spectral information, improve the detected cadence and avoid overlapping. The approach is inseparable from the design of optical system for multi-slits imaging spectrograph and the optimization of narrow-band multilayer structure.

3 Optical system design and performance

3.1 Optical system design

The optical system of a multi-slits imaging spectrograph, as shown in Figure 2, consists of an entrance filter, a primary mirror, a multi-slits element, a grating, a rear filter and a detector. The multi-slits element contains several distantly separated slits, as shown in the inset figure below, instead of a single slit as in EIS, or thirty-seven closely separated slits as in MUSE. The challenge is to determine the optimal number of slits to achieve a balanced cadence for a global FOV raster and less influence of spectral overlapping. A large number of slits can divide the entire FOV into more slices, increasing the cadence. However, this may introduce severe overlap from adjacent slits in the case of a continuous spectral range with multiple spectral lines. A small number of slits can effectively avoid overlapping, but each slit will require more time to scan a larger field of view. In addition, the transmission efficiency and bandwidth of the optical element, which depend on the materials and parameters of the multilayer mirror and grating, will also affect the overlap from adjacent slits. The optical system

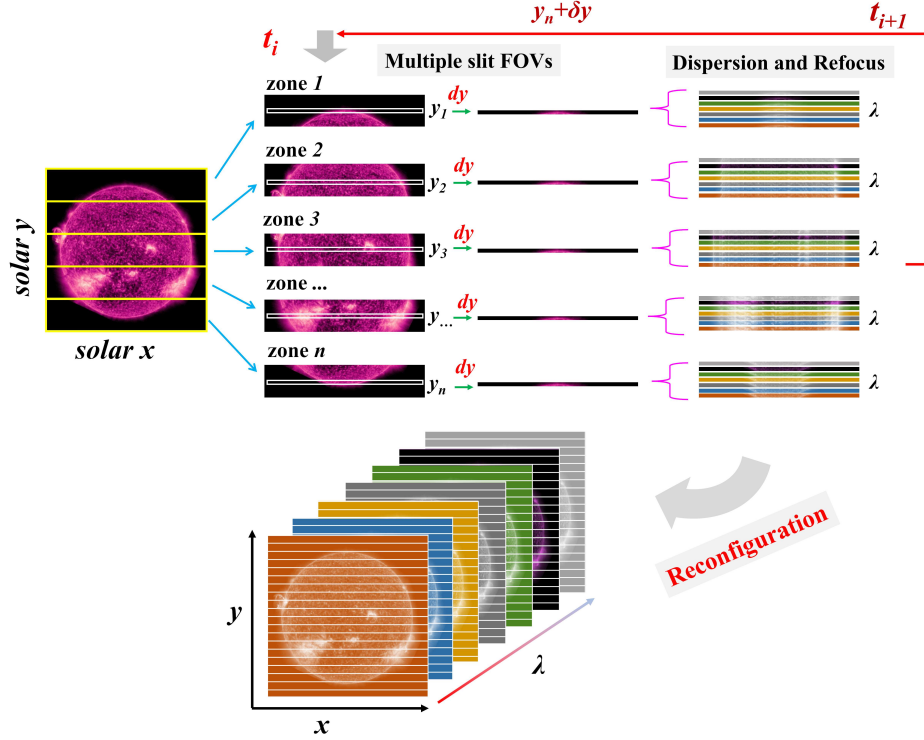


Fig. 1 Overview of detection methods. The solar image in the example is from the Solar Upper Transition Region Imager (SUTRI, Bai et al, 2023), detected at 17:49:12 UT on September 23rd, 2022.

parameters also need to be optimized to meet the spatial resolution and spectral resolving power.

We first provide a general multi-slits EUV imaging spectrometer design process through a series of basic physical relationships between optical performance and system structural parameters. The spectral spacing $d\lambda$ of adjacent slits depends on the effective focal length F of the optical system, FOV spacing of slits $\Delta\theta$, and the reciprocal linear dispersion σ . In order to avoid overlapping, the $\Delta\lambda$ of the observed bands should be smaller than the spectral spacing $d\lambda$ of adjacent slits (Equation (1)). The smaller the spot size of the image plane or pixel size of the detector, the better the spatial resolution δ (Equation (2)) and the spectral resolving power R (Equation (3)). These relationships, as well as the specific parameters for the observations, are described as follows:

$$d\lambda = F \times \tan \frac{\Phi}{n} \times \sigma > 1.5 \text{ nm}, \quad (1)$$

$$\delta = \arctan \frac{\max(ss, sp)}{F} \approx \frac{\max(ss, sp)}{F} \times 206265 \approx 6'', \quad (2)$$

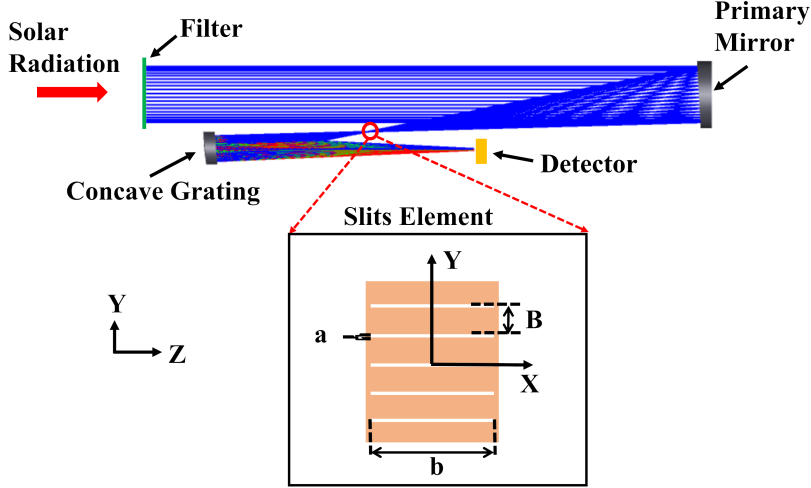


Fig. 2 Schematic layout of optical system

$$R = \frac{\lambda_0}{\Delta\lambda_0} = \frac{\lambda_0}{\max(ss, sp) \times \sigma} > 500 \quad (\lambda_0 = 19.0 \text{ nm}). \quad (3)$$

where $\sigma = \lambda_\sigma/x_\sigma$, which express the spectral range included in a unit distance on the image plane. It is a parameter used to evaluate the degree of spectral dispersion. ss represents the spot size of the image plane, coupling diffraction effects and geometric aberration. sp denotes the sampling period of the detector, and 206265 is the conversion factor from radians to arcseconds.

The performance of an optical system depends on the optical elements. The reciprocal linear dispersion, σ , is determined by the grating parameters (Equation (4)). The effective focal length of the optical system F (Equation (5)) depends on the focal length of the primary mirror f_0 and the magnification of the grating m_g (Equation (6)). These parameters can be expressed more specifically as:

$$\sigma = \frac{p \cos \beta(\lambda) \cos(\gamma)}{mr_1}, \quad (4)$$

$$F = f_0 \times m_g, \quad (5)$$

$$m_g = \frac{r_1}{r_0}. \quad (6)$$

where p is the grating period, $\beta(\lambda)$ is the diffraction angle, γ is the angle between the detector plane and the incident light, m is the diffraction order, r_1 is the distance from the grating to the detector, and r_0 is the distance from the slits to the grating.

Considering the fabrication capability of practical EUV optical elements, some parameters are limited to a specific range. The detector adopts a 2048×2048 pixel array with a pixel size of $11 \mu\text{m} \times 11 \mu\text{m}$, and 3 pixels will be the sampling period to better satisfy the Nyquist-Shannon sampling theorem (Equation (7)). The primary

mirror is an off-axis parabolic mirror with a diameter of 150 mm (Equation (8)), chosen as a compromise between the effective collecting area and off-axis aberration of the system. In addition, our detection scheme is not for extreme resolution and is a narrow observation band, so an ellipsoidal grating with uniform-line-space can meet the requirements and is preferred. The line density of the grating is further limited to no more than $3600 \text{ line} \cdot \text{mm}^{-1}$, meaning the grating period p is greater than 277.77 nm (Equation (9)). The grating magnification ranges between 1.5 and 2.5 (Equation (10)), which determines the slit width a in combination with the pixel size. The limitations are listed as follows:

$$sp = 11 \mu\text{m} \times 3 = 33 \mu\text{m}, \quad (7)$$

$$D = 150 \text{ mm}, \quad (8)$$

$$p > 277.77 \text{ nm}, \quad (9)$$

$$1.5 < m_g < 2.5, \quad (10)$$

Off-axis aberration, which seriously degrades optical performance, is another issue that needs to be overcome. Many studies have contributed to the analysis of off-axis aberrations for a EUV imaging spectrograph with concave grating (Beutler, 1945; Harada et al, 1995, 1998; Thomas, 2003, 2004). It is still extremely difficult to obtain the minimum aberration by solving parametric equations analytically due to its multi-parameter nonlinear coupling process. We can, nevertheless, obtain the best parameters optimized through numerical simulation methods. The relationships and constraints mentioned above are crucial references for establishing the initial parameters and optimization objectives of a numerical model. In our work, optical simulation software Zemax OpticStudio is used to reduce the aberrations and to minimize the spot size as much as possible for the wavelength of 18.3 nm, 19.0 nm and 19.8 nm. Multiple field of view points, including $(0', 0')$, $(0', -/+10')$, $(0', -/+20')$, $(-/+10', 0')$ and $(-/+20', 0')$, are used in the optimized merit function to achieve better resolution across all observation fields. Optimized parameters mainly include the distance from the slits to the grating r_0 , the distance from the grating to the detector r_1 , the grating line density, the grating surface shape parameters and the detector angle, etc. The specific parameters of the optical system and elements after optimization are shown in Table 2.

3.2 Optical performance

In our design, the full-disk FOV is divided into five regions, i.e., the number of slits n is 5, and the spacing between two nearby slits in the FOV, denoted as $\Delta\theta$, is $10'$. By using ray tracing, the position distribution of light at different wavelengths from each slit FOV can be obtained on the image plane (Figure 3). The five slits are positioned at $y = -20', -10', 0', 10', \text{ and } 20'$. For each slit, the central wavelength is 19.0 nm, and the light spots at 18.3 nm–19.8 nm are successively separated. At the same time, the light spots from the adjacent slits are not mixing with each other. For example,

Table 2 Specific parameters of the optical system and elements

System and Elements	Parameters	Optimization Value
System design	Raster FOV $\Phi/^\circ$	$40' \times 50'$ in 200 raster steps of $3''$ with 5 slits
	Wavelength λ/ nm	18.3, 19.0 19.8
	Effective Focal Length F/ mm	1533.492
	Reciprocal linear dispersion $\sigma/ (\text{nm} \cdot \text{mm}^{-1})$	0.398
	Slit number n	5
	Slit space $\Delta\theta/^\circ$	10
	Slit spectral space $d\lambda/ \text{nm}$	1.71
	Slit width $a/ \mu\text{m}$	15
Slit FOV $dy/ ''$	3.43	
Primary mirror parameter	Mirror type	Off-axis parabolic mirror
	Diameter D/ mm	150 mm
	Radius of curvature R_0/ mm	1800
	Off-axis distance $/ \text{mm}$	100
Grating parameter	Conic	-1
	Grating type	Ellipsoidal uniform-line-space grating
	Diameter $/ \text{mm}$	80
	Line density $/ (\text{line} \cdot \text{mm}^{-1})$	3595
	Grating period p/ nm	278.16
	Surface Value	a=0.001781;b=0.001779;c=605.826
	Diffraction order m	-1
	Distance from the slits to the grating r_0/ mm	413.80
	Distance from the grating to the detector r_1/ mm	700.78
Grating magnification m_g	1.69	
Detector design	Pixel arrays	2048×2048
	Pixel size $/ (\mu\text{m} \times \mu\text{m})$	11×11
	Spatial sampling per pixel $/ ''$	1.46
	Spectral sampling per pixel $/ \text{nm}$	0.0043
	System spatial resolution $/ ''$	4.40
	System spectral resolution $/ \text{nm}$	0.013
System spectral resolving power $\lambda_0/\Delta\lambda_0$	1461($\lambda_0 = 19.0 \text{ nm}$)	

the 19.8 nm light spot from slit **1** does not overlap with the 18.3 nm light spot from slit **2**. The results indicate that there is no overlap from the adjacent slits for the input spectral range ($\Delta\lambda = 1.5 \text{ nm}$).

The Airy spot radius of the optical system is about $0.23 \mu\text{m}$ at the wavelength of 19 nm, which is much smaller than the radius caused by aberration. The spherical aberration of the grating is the main factor affecting the performance of the optical system, while the coma aberration from the primary mirror and grating is balanced with each other. In addition, there is a little pincushion type distortion in the image plane, resulting in a maximum spectral curvature of about 0.22%. More analysis of spot size at the image plane can refer to the ray tracing results. Figure 4 (a) and (b) show the root mean square (RMS) spot diameter of three different wavelengths in the five off-axis FOVs along the x direction and y direction, respectively. The spot diameter at the center of FOV is the smallest, and it gradually increases as the deviation from the center of FOV becomes larger in either the x or y direction. At the wavelength of 19.0 nm, the spot diameter in the central FOV is about $8.62 \mu\text{m}$, and the spot size of the off-axis FOV at $-/+20'$ in the x and y directions is $29.34/29.34 \mu\text{m}$ and $13.26/33.09 \mu\text{m}$, respectively. In the case of 18.3 nm and 19.8 nm, the tendency in

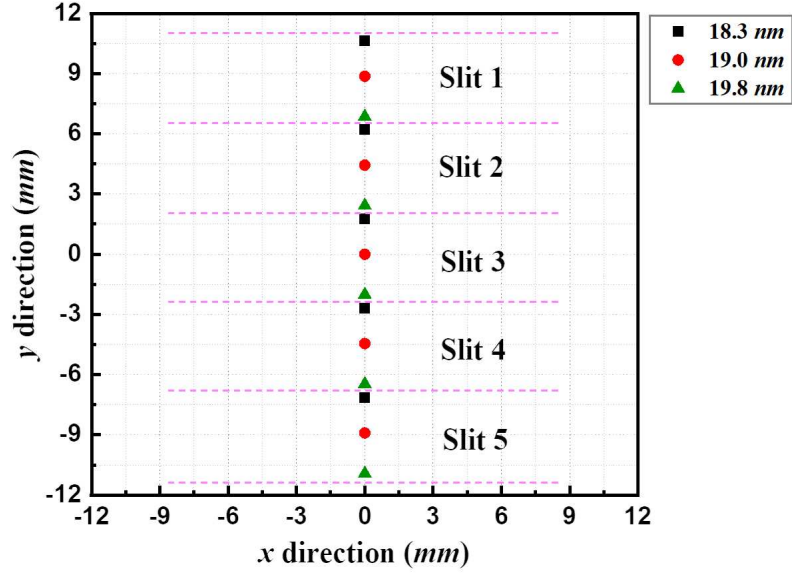


Fig. 3 Position distribution of light spots of different wavelengths at the image plane

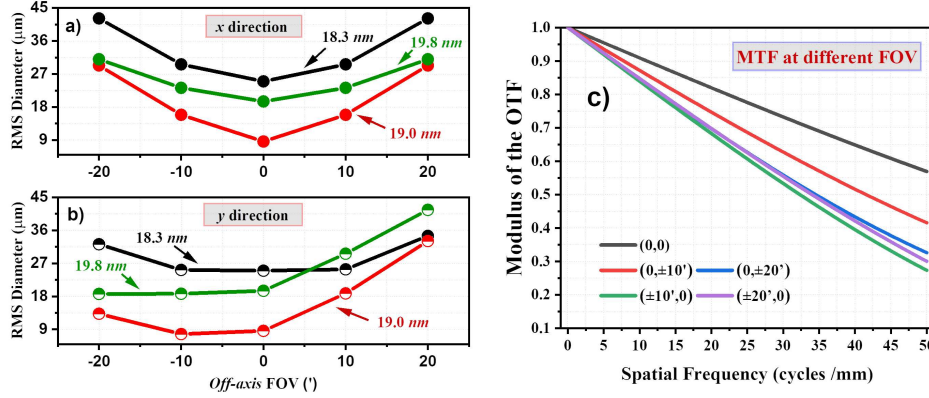


Fig. 4 Performance of optical systems in different off-axis FOV: Spot RMS diameter of different wavelengths of x direction (a) and y direction (b) and MTF curves of the image plane (c).

spot size with off-axis FOV are consistent, but the magnitudes are greater, influenced by grating aberration. Figure 4(c) presents the Modulation Transfer Function (MTF) curves of the image plane at different off-axis FOV. The curve represents the average value for each FOV at different wavelengths. At a frequency of about 30.3 cycles/mm (3 pixels per period), the MTF values for all FOVs exceed 0.52, meeting the detection requirements.

Figure 5 illustrates the spatial and spectral resolution of the three different wavelengths in the five off-axis FOVs, calculated using Eq.(3) and averaging the x and y directions. The results show that both the spatial and spectral resolution decrease

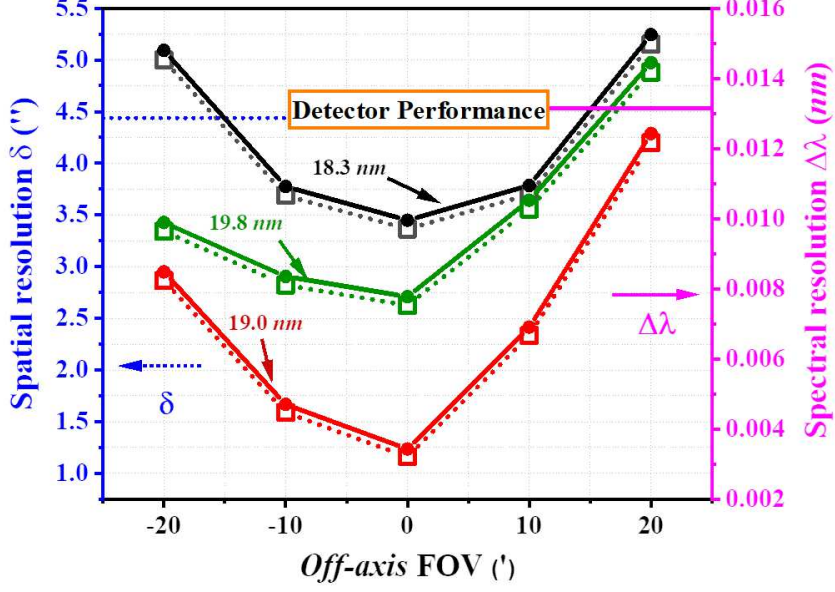


Fig. 5 Spatial resolution (dot lines) and spectral resolution (solid lines) of different wavelengths in different off-axis FOV, detector performance based on the sampling period also marked with blue dots and purple solid lines

with the deviation from the center FOV. The resolution corresponding to three pixels sampling with the detector is also indicated in Figure 5. In other words, the resolution of the optical system is limited by the three pixel sampling. The spatial resolution of the optical system is about $4.4''$, and the spectral resolution is about 0.013 nm (i.e., the spectral resolving power exceeds 1461). The worst spatial and spectral resolutions are $5.1''$ and 0.015 nm (i.e., the spectral resolving power is greater than 1266), respectively. The spatial resolution of the scanning direction also needs to consider the slit width and scanning step. Our scheme has a slit width of $3.43''$, which means the spatial resolution in the scanning direction is about $6.86''$.

3.3 Effective Areas

The effective area is another key parameter of the optical system that determines the number of received photons or the signal-to-noise ratio (S/N) for a single exposure. On the one hand, the bandwidth of the effective area needs to be large enough to cover the observation band. On the other hand, the sideband of effective area needs to suppress to avoid overlapping caused by excess radiation. The effective area $e(\lambda)$ of the optical system depends on the transmission efficiency of each optical element at different wavelengths, which can be expressed as:

$$e(\lambda) = A \times T_{ff}(\lambda) \times R(\lambda) \times T_{rf}(\lambda) \times E(\lambda) \times Q(\lambda). \quad (11)$$

where A is the effective light collecting area of the optical system, $T_{ff}(\lambda)$ and $T_{rf}(\lambda)$ are the transmissions of the front and rear filters, respectively. $R(\lambda)$ represents the

reflectance of the primary mirror coated with multilayers. $E(\lambda)$ is the diffraction efficiency of multilayer gratings, which includes both the groove efficiency and the reflectivity of the multilayer coatings, and $Q(\lambda)$ is the detector quantum efficiency.

The material of the front filter and the spectrometer entrance filter is Al thin-films, which have high transmittance in the band of 17.1–25.0 nm and have been widely used in many EUV solar instruments such as EIS (Korendyke et al, 2006) and Hi-C (Rachmeler et al, 2019). The design thickness of both Al filters is 250 nm, while 5 nm of aluminum oxide is applied on both sides to adapt to the actual situation. The transmittance curve of the filters is calculated using IMD software (Windt, 1998), as shown in Figure 6(a). The results show that the transmittance in the 18.3–19.8 nm band is greater than 53%.

The multilayer structure is designed for the primary mirror to enhance the transmission efficiency of the target waveband. In the 18–20 nm band, an Al and B₄C material combination is selected, and a thin Mo layer is added to improve the interface roughness (Delmotte et al, 2013; Corso and Pelizzo, 2019). The structural parameters of Al/Mo/B₄C multilayers, including d-spacing, the number of multilayer N , etc., are optimized using IMD software to achieve high reflectivity in the observation band while reducing the sideband. The optimized multilayer structure is Al/Mo/B₄C [5.1 nm/3 nm/2 nm], and the multilayer number N is 15. Additionally, a B₄C protective layer with a thickness of 10 nm is added on top to prevent oxidation and ion bombardment from solar wind. The reflectance curve at the incident angle of 3.17° is shown in Figure 6(a), where the interface roughness of the calculation model is set to 0.6 nm. The results indicate that the reflectance at 19.3 nm is about 43.5%, while the values are 27.9% and 27.2% at the wavelengths of 18.3 nm and 19.8 nm, respectively.

The optimized multilayer structure is also combined with the grating. Based on the incident angle and multilayer structure, the grating groove depth is determined to be 4.76 nm, and the duty cycle is 0.5. Figure 6(a) shows the diffraction efficiency curves of the -1^{st} order of the multilayer grating as a function of wavelength. These curves are calculated numerically using rigorous coupled wave analysis (RCWA). The results indicate that the diffraction efficiency of the multilayer grating at a wavelength of 19.3 nm is approximately 16.5%.

Finally, the effective area $e(\lambda)$ of the whole system can be calculated using Equation (11) with the efficiency values of the elements obtained above. The result is shown in Figure 6(b). The quantum efficiency of the detector is set at 0.5, while the reduction factor of the actual multilayer grating efficiency is 0.85. This reduction factor accounts for the interface roughness of the multilayers and the variation in grating groove, compared to the ideal calculation model. The effective area at 19.3 nm is about 1.61 cm², which is 5 times larger than that of EIS. The values at 18.3 nm and 19.8 nm are both approximately half of the peak (0.80 cm²), while the effective areas are reduced to 0.035 cm² and 0.049 cm² at the wavelengths of 17.5 nm and 20.5 nm, respectively. The small overlaps from the adjacent slits could be separated algorithmically.

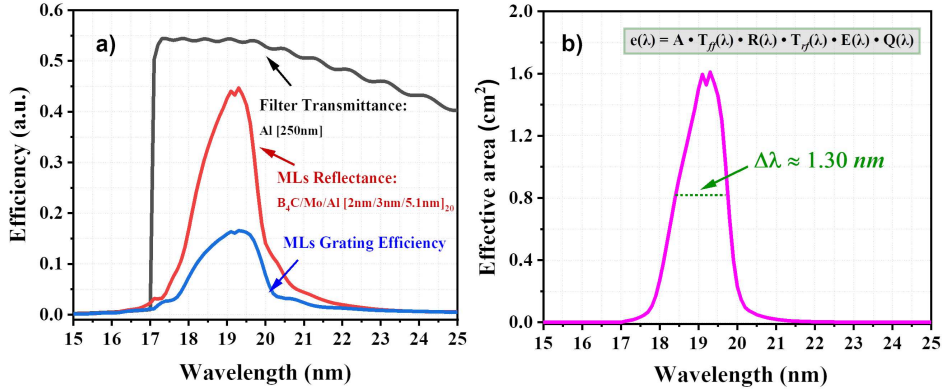


Fig. 6 Theoretical calculation efficiency curve of elements (a) and the effective area of the optical system (b).

Table 3 Calculated solar radiation and detection photon numbers of the instrument

Ion and Wavelength Å	Solar radiation $\times 10^{12}$ photons cm^{-2} s^{-1} sr^{-1} Å^{-1}		Detected photon number photons s^{-1} pixel^{-1}	
	2-5	AR	QS	AR
Fe VIII 185.21 Å	34.87	5.14	73.0	10.78
Fe X 184.54 Å	54.17	4.26	98.5	7.7
Fe XI 188.22 Å	68.80	4.09	195.5	11.6
Fe XII 186.89 Å	88.74	4.11	207.9	9.6
Fe XII 193.51 Å	116.92	4.37	424.0	15.8
Fe XII 195.12 Å	174.88	8.02	573.9	26.3

Note. The calculation of solar radiation uses two standard CHIANTI differential emission measures (AR and QS), assuming an electron density of 10^9 cm^{-3} . We also assume ionization equilibrium and adopt the coronal abundance from Schmelz et al 2012. The spectral line shape adopts Gaussian profile and the line width of about 0.2 Å is given by a combination of thermal broadening and instrumental broadening.

4 End-to-end optical response and photon budget

It is critically important to evaluate the instrument response to solar radiation to better understand its sensitivity under various measurement conditions. Using the synthetic spectra and the effective areas, the photon numbers registered in each detector pixel per second $N(\lambda)$ (photons s^{-1} pixel^{-1}) can be expressed as:

$$N(\lambda) = I(\lambda) \times e(\lambda) \times \delta_{sr} \times \delta_{\lambda} \quad (12)$$

where $I(\lambda)$ (photons cm^{-2} s^{-1} sr^{-1} Å^{-1}) is the intensity of the solar radiation calculated with CHIANTI (Dere et al, 1998; Young et al, 2003), $e(\lambda)$ is the effective area including all factors from Equation (11), and δ_{sr} and δ_{λ} represent the solid angle and spectral resolution per pixel, respectively.

Table 3 presents the input solar radiation and received photon numbers per pixel of six typical lines (Fe VIII 185.21 Å, Fe X 184.54 Å, Fe XI 188.22 Å, Fe XII 186.89 Å, Fe XII 193.51 Å, and Fe XII 195.12 Å) in AR and QS. We set a single detected time

of 1.5 s (including exposure time of 1.3 s and raster scan time of 0.2 s by rotating the primary mirror) and a raster step of $3''$. To scan the whole FOV with 5 slits, we need $(3000''/5)/3'' = 200$ scanning steps and complete the scan of the whole FOV within $200 \times 1.5 \text{ s} = 300 \text{ s}$. For the detection in AR, the typical photon numbers are greater than $95 \text{ photons s}^{-1} \text{ pixel}^{-1}$ with a 1.3 s exposure time for all spectral lines. For the detection in QS, the typical photon numbers of the strong radiation lines (Fe XII 193.51 Å, Fe XII 195.12 Å, etc.) are within $20\text{--}32 \text{ photons s}^{-1} \text{ pixel}^{-1}$ for a single exposure time. While for the detection of weak radiation lines (Fe VIII 185.21 Å, Fe XI 188.22 Å, etc.) in QS, we could sacrifice the temporal resolution to increase the S/N ratio. Either the multi-frames integration methods or setting a longer exposure time can be adopted. For the regions with flares, the exposure time should be set much lower to avoid saturation.

Although we avoid overlapping in the design of optical system for the input spectral range ($\Delta\lambda = 1.5 \text{ nm}$), there is still small overlapping due to the unavoidable sideband of the effective area. A decomposition method is employed to extract spectra from each slit in the observed spectra and generate the global coronal map. The method, which adheres to the basic inversion framework outlined by Cheung et al (2015; 2019), has been evaluated for a multi-slit extreme ultraviolet imaging spectrograph by Chan et al 2024. Chan et al 2024 utilized a numerical model (from Predictive Science Inc.) as the observation spectrum (ground truth) to examine the influence of spectra overlapping. The results presented here are achieved by executing the program in combination with the parameters of the instrument. The noticeable difference between the two schemes is slit separation on the plane of sky and spectral spacing of the inter-slits on the spectrogram. We optimized the spectral spacing to 17.1 Å to avoid overlapping from adjacent slits as much as possible, while Chan’s scheme had a inter-slit spacing of 1 Å mainly to verify the decomposition method. In Figure 7(a), we synthesized the global intensity map of the Fe XII 195.12 Å. The structures of coronal loops from AR and CHs are clearly resolved. The bottom panel of Figure 7(b) displays the synthesized (solid lines) and inverted spectra (dot lines) from five slit pieces marked with white squares in Figure 7(a), and the top panel showcases the zoom-in spectrum from slits **2** to **4**. Notably, in Figure 7(b), there is an inevitable overlap of spectra from adjacent slits, denoted by a gray bar. Due to significant variations in radiation intensity, several lines from slit **2** (located near the AR) exhibit comparable strength to the primary lines from slit **3** (located near the coronal hole). Limited by computing resources, the inversion here primary prioritizes the acquisition of accurate information for six primary lines. Other lines, such as 183.93 Å on the left edge of slit **3** (at the detector position of about -2.67 mm), may not include potential parameters during the inversion process, resulting in large deviation. One possible solution in the future would be to extend our parameter space of the response matrix to obtain more accurate information, while this would result in increased computation time.

5 Conclusions

The paper describes a method to optimize multi-slit extreme ultraviolet imaging spectrograph for global coronal plasma diagnostic with high cadence. Five narrow slits

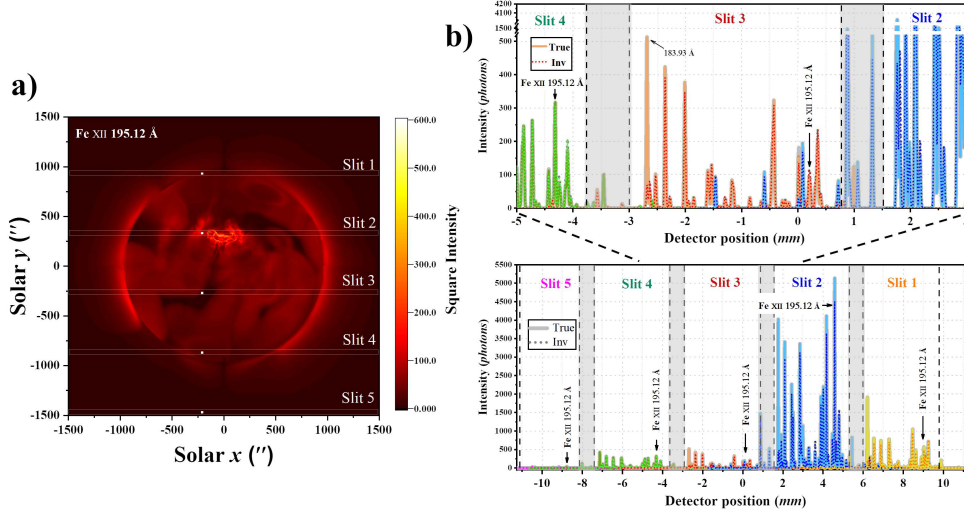


Fig. 7 (a) shows the synthesized global intensity map for Fe XII 195.12 Å. Bottom panel of (b) shows total spectra from 5 slits marked with white squares in Figure 7(a) and top panel of (b) shows the zoom-in spectrum from slits 2 to 4. For improved clarity, two breakpoints (the first one ranges from 520 to 1400, and the second one ranges from 1600 to 4000) have been set for the ordinate of top panel in (b).

are designed to divide the entire solar field of view, which can increase the cadence by 5 times relative to a single slit and raster scan full-disk with 5 minutes. Considering the fabrication capability of practical EUV optical elements and the scientific requirements, the parameters are optimized in the spectral range of 18.3–19.8 nm with an aperture diameter of 150 mm. The spatial resolution of optical system is better than $4.4''$ and the spectral resolving power exceeding 1461. The Al/Mo/B₄C multilayer structure is optimized to maximize the efficiency of the reflector and grating in the observation band, resulting a peak effective area of about 1.60 cm² at 19.3 nm. Finally, the instrument performance is evaluated by calculating the photon numbers and inverting the spectra to obtain a global coronal map. This work offers an innovative approach for full-disk corona spectral diagnostics. The method is also useful for the design of a multi-slit imaging spectrograph worked at the other EUV wavelength and estimating its performance.

In order to realize our detection scheme, some practical challenges would be further explored in the future. First, it is crucial that the groove shaped replication growth of multilayer on ellipsoidal gratings with a line density of about 3600 line · mm⁻¹. There have been many studies on the improvement of coating process of multilayer gratings (e.g., Voronov et al, 2012; Feng et al, 2021). Recently, Mahmoud et al 2022 reported the preparation and characterization of Al/Mo/SiC multilayer lamellar gratings with line densities of 3600 line · mm⁻¹. The results indicate that the diffraction efficiency decreased for a large multilayer number due to the deviation of grating profile. Therefore, in the future, some measures, including multilayer design and coating process improvement, are key to achieve high efficiency ellipsoidal gratings with high line density. Then high precision image stabilization system and scanning mechanism

are also the key to realize full-disk FOV detection by raster scan. The slit FOV in our scheme is about $3.43''$, which means that the accuracy of the image stabilization system and the error of scanning step should be better than $0.3''$. The raster scan time of the instrument is about 0.2 s, resulting in the response time of the image stabilization system and scanning mechanism should be less than 100 ms. Finally, it is a very complicated process to reconstruct full-disk FOV spectral imaging information with many slit scanning fragments. Spectral extraction is the result of evaluating overlapping and decomposition method. Global coronal imaging is the coupling of decomposition methods with slit width, scan step, etc.

Acknowledgements. This work was supported by National Key R&D Program of China No. 2021YFA1600500, National Natural Science Foundation of China No. 12303088. CHIANTI is a collaborative project involving George Mason University, the University of Michigan (USA), University of Cambridge (UK) and NASA Goddard Space Flight Center (USA).

Declarations

- Funding This work was supported by National Key R&D Program of China No. 2021YFA1600500, National Natural Science Foundation of China No. 12303088.
- Competing interests The authors declare no competing interests.
- Ethics approval and consent to participate Not applicable.
- Consent for publication The authors confirm that this article has not been previously published in any journal.
- Data availability Not applicable.
- Materials availability Not applicable.
- Code availability Not applicable.
- Author contribution Conceptualization: Yufei Feng, Xianyong Bai, Hui Tian. Methodology: Yufei Feng, Xianyong Bai, Hui Tian. Formal analysis and investigation: Sifan Guo, Lami Chan, Qi Yang, Wei Duan. Writing - original draft preparation: Yufei Feng Writing - review and editing: Xiaoming Zhu, Xiao Yang, Zhiwei Feng, and Zhiyong Zhang. Supervision: Hui Tian, Yuanyong Deng.

References

- Anan T, Jaeggli S, Lin H, et al (2024) Implementation of the $36\ \mu\text{m}$ machined image slicer integral field unit for DKIST/DL-NIRSP. In: Bryant JJ, Motohara K, Vernet JRD (eds) Ground-based and Airborne Instrumentation for Astronomy X, International Society for Optics and Photonics, vol 13096. SPIE, p 1309626, <https://doi.org/10.1117/12.3019649>, URL <https://doi.org/10.1117/12.3019649>
- Bai X, Tian H, Deng Y, et al (2023) The Solar Upper Transition Region Imager (SUTRI) Onboard the SATech-01 Satellite. *Research in Astronomy and Astrophysics* 23(6):065014. <https://doi.org/10.1088/1674-4527/accc74>, arXiv:2303.03669 [astro-ph.SR]

- Beutler HG (1945) The theory of the concave grating. *Journal of the Optical Society of America* (1917-1983) 35(5):311
- Brooks DH, Ugarte-Urra I, Warren HP (2015) Full-sun observations for identifying the source of the slow solar wind. *Nature communications* 6:5947. <https://doi.org/10.1038/ncomms6947>, URL <https://europepmc.org/articles/PMC4354106>
- Calcines Rosario A, Reid HAS, Matthews S, et al (2023) Sisa: The first extreme-ultraviolet solar integral field spectrograph using slicers. <https://doi.org/10.20944/preprints202311.1854.v1>, URL <https://doi.org/10.20944/preprints202311.1854.v1>
- Chamberlin PC, Gong Q (2016) An integral field spectrograph utilizing mirrorlet arrays. *Journal of Geophysical Research (Space Physics)* 121(9):8250–8259. <https://doi.org/10.1002/2016JA022487>
- Chan L, Tian H, Liu X, et al (2024) Global Coronal Plasma Diagnostics Based on Multislit Extreme-ultraviolet Spectroscopy. *apj* 967(2):162. <https://doi.org/10.3847/1538-4357/ad4114>, [arXiv:2404.13120](https://arxiv.org/abs/2404.13120) [astro-ph.SR]
- Cheung MCM, Boerner P, Schrijver CJ, et al (2015) Thermal Diagnostics with the Atmospheric Imaging Assembly on board the Solar Dynamics Observatory: A Validated Method for Differential Emission Measure Inversions. *apj* 807(2):143. <https://doi.org/10.1088/0004-637X/807/2/143>, [arXiv:1504.03258](https://arxiv.org/abs/1504.03258) [astro-ph.SR]
- Cheung MCM, De Pontieu B, Martínez-Sykora J, et al (2019) Multi-component Decomposition of Astronomical Spectra by Compressed Sensing. *apj* 882(1):13. <https://doi.org/10.3847/1538-4357/ab263d>, [arXiv:1902.03890](https://arxiv.org/abs/1902.03890) [astro-ph.SR]
- Cheung MCM, Martínez-Sykora J, Testa P, et al (2022) Probing the Physics of the Solar Atmosphere with the Multi-slit Solar Explorer (MUSE). II. Flares and Eruptions. *apj* 926(1):53. <https://doi.org/10.3847/1538-4357/ac4223>, [arXiv:2106.15591](https://arxiv.org/abs/2106.15591) [astro-ph.SR]
- Corso AJ, Pelizzo MG (2019) Extreme ultraviolet multilayer nanostructures and their application to solar plasma observations: A review. *Journal of nanoscience and nanotechnology* 19 1:532–545. URL <https://api.semanticscholar.org/CorpusID:53528482>
- Culhane JL, Harra LK, James AM, et al (2007) The EUV Imaging Spectrometer for Hinode. *solphys* 243(1):19–61. <https://doi.org/10.1007/s01007-007-0293-1>
- De Pontieu B, Martínez-Sykora J, Testa P, et al (2020) The Multi-slit Approach to Coronal Spectroscopy with the Multi-slit Solar Explorer (MUSE). *apj* 888(1):3. <https://doi.org/10.3847/1538-4357/ab5b03>, [arXiv:1909.08818](https://arxiv.org/abs/1909.08818) [astro-ph.IM]
- De Pontieu B, Testa P, Martínez-Sykora J, et al (2022) Probing the Physics of the Solar Atmosphere with the Multi-slit Solar Explorer (MUSE). I. Coronal Heating.

- apj 926(1):52. <https://doi.org/10.3847/1538-4357/ac4222>, arXiv:2106.15584 [astro-ph.SR]
- Del Zanna G, Mason HE (2018) Solar UV and X-ray spectral diagnostics. *Living Reviews in Solar Physics* 15(1):5. <https://doi.org/10.1007/s41116-018-0015-3>, arXiv:1809.01618 [astro-ph.SR]
- Delmotte F, Meltchakov E, de Rossi S, et al (2013) Development of multilayer coatings for solar orbiter EUV imaging telescopes. In: Fineschi S, Fennelly J (eds) *Solar Physics and Space Weather Instrumentation V*, p 88620A, <https://doi.org/10.1117/12.2036050>
- Dere KP, Landi E, Mason HE, et al (1998) CHIANTI - an Atomic Database For Emission Lines Paper I: Wavelengths Greater than 50 Angstroms. In: Brandt JC, Ake TB, Petersen CC (eds) *The Scientific Impact of the Goddard High Resolution Spectrograph*, p 390
- Domingo V, Fleck B, Poland AI (1995) The SOHO Mission: an Overview. *solphys* 162(1-2):1–37. <https://doi.org/10.1007/BF00733425>
- Dominguez-Tagle C, Collados M, Lopez R, et al (2022) First Light of the Integral Field Unit of GRIS on the GREGOR Solar Telescope. *Journal of Astronomical Instrumentation* 11(3):2250014. <https://doi.org/10.1142/S2251171722500143>, arXiv:2206.14294 [astro-ph.IM]
- Feng Y, Huang Q, Zhuang Y, et al (2021) Mo/Si lamellar multilayer gratings with high efficiency and enhanced resolution for the x-ray region of 1000-1700eV. *Optics Express* 29(9):13416. <https://doi.org/10.1364/OE.422483>
- Fox JL (2011) Snapshot imaging spectroscopy of the solar transition region: The Multi-Order Solar EUV Spectrograph (MOSES) sounding rocket mission. PhD thesis, Montana State University System
- Golub L, Cheimets P, DeLuca EE, et al (2020) EUV imaging and spectroscopy for improved space weather forecasting. *Journal of Space Weather and Space Climate* 10:37. <https://doi.org/10.1051/swsc/2020040>
- Harada T, Sakuma H, Ikawa Y, et al (1995) Design of high-resolution XUV imaging spectrometer using spherical varied line-space grating. In: Fineschi S (ed) *X-Ray and EUV/FUV Spectroscopy and Polarimetry*, pp 107–115, <https://doi.org/10.1117/12.224928>
- Harada T, Sakuma H, Takahashi K, et al (1998) Design of a High-Resolution Extreme-Ultraviolet Imaging Spectrometer with Aberration-Corrected Concave Gratings. *ao* 37(28):6803–6810. <https://doi.org/10.1364/AO.37.006803>

- Korendyke CM, Brown CM, Thomas RJ, et al (2006) Optics and mechanisms for the Extreme-Ultraviolet Imaging Spectrometer on the Solar-B satellite. *ao* 45(34):8674–8688. <https://doi.org/10.1364/AO.45.008674>
- Laurent GT, Hassler DM, Deforest C, et al (2016) The Rapid Acquisition Imaging Spectrograph Experiment (RAISE) Sounding Rocket Investigation. *Journal of Astronomical Instrumentation* 5(1):1640006-34. <https://doi.org/10.1142/S2251171716400067>
- Lin H, Sukegawa T, Bonnet MB, et al (2022) MISI-36: Machined image slicer integral field units for the Diffraction-Limited Near-IR Spectropolarimeter. In: Navarro R, Geyl R (eds) *Advances in Optical and Mechanical Technologies for Telescopes and Instrumentation V*, International Society for Optics and Photonics, vol 12188. SPIE, p 1218828, <https://doi.org/10.1117/12.2629979>, URL <https://doi.org/10.1117/12.2629979>
- Lu H, Tian H, chao Chen H, et al (2023) Full velocities and propagation directions of coronal mass ejections inferred from simultaneous full-disk imaging and sun-as-a-star spectroscopic observations. *The Astrophysical Journal* 953(1):68. <https://doi.org/10.3847/1538-4357/acd6a1>, URL <https://dx.doi.org/10.3847/1538-4357/acd6a1>
- Mahmoud AHK, de Rossi S, Meltchakov E, et al (2022) Al/Mo/SiC multilayer diffraction gratings with broadband efficiency in the extreme ultraviolet. *Optics Express* 30(21):38319. <https://doi.org/10.1364/OE.468568>
- Mariska JT, Warren HP, Ugarte-Urra I, et al (2007) Hinode EUV Imaging Spectrometer Observations of Solar Active Region Dynamics. *pasj* 59:S713. <https://doi.org/10.1093/pasj/59.sp3.S713>, [arXiv:0708.4309](https://arxiv.org/abs/0708.4309) [astro-ph]
- Rachmeler LA, Winebarger AR, Savage SL, et al (2019) The High-Resolution Coronal Imager, Flight 2.1. *solphys* 294(12):174. <https://doi.org/10.1007/s11207-019-1551-2>, [arXiv:1909.05942](https://arxiv.org/abs/1909.05942) [astro-ph.SR]
- Reeves K, Seaton DB, Golub L, et al (2022) ECCCO: The EUV CME and Coronal Connectivity Observatory. In: *AGU Fall Meeting Abstracts*, pp SH23A–06
- Schmelz JT, Reames DV, von Steiger R, et al (2012) Composition of the Solar Corona, Solar Wind, and Solar Energetic Particles. *apj* 755(1):33. <https://doi.org/10.1088/0004-637X/755/1/33>
- SPICE Consortium, Anderson M, Appourchaux T, et al (2020) The Solar Orbiter SPICE instrument. An extreme UV imaging spectrometer. *aap* 642:A14. <https://doi.org/10.1051/0004-6361/201935574>, [arXiv:1909.01183](https://arxiv.org/abs/1909.01183) [astro-ph.IM]

- Sukegawa T, Lin H, Bonnet M (2023) Ultra-compact machined slicer IFU. In: Minoglou K, Karafolas N, Cugny B (eds) Society of Photo-Optical Instrumentation Engineers (SPIE) Conference Series, p 127773V, <https://doi.org/10.1117/12.2690568>
- Thomas RJ (2003) Toroidal varied-line space (TVLS) gratings. In: Keil SL, Avakyan SV (eds) Innovative Telescopes and Instrumentation for Solar Astrophysics, pp 411–418, <https://doi.org/10.1117/12.460375>
- Thomas RJ (2004) Elliptical varied line-space (EVLS) gratings. In: Hasinger G, Turner MJL (eds) UV and Gamma-Ray Space Telescope Systems, pp 755–762, <https://doi.org/10.1117/12.552131>
- Tian H, Harra L, Baker D, et al (2021) Upflows in the Upper Solar Atmosphere. *solphys* 296(3):47. <https://doi.org/10.1007/s11207-021-01792-7>, [arXiv:2102.02429](https://arxiv.org/abs/2102.02429) [astro-ph.SR]
- Tousey R, Bartoe JDF, Brueckner GE, et al (1977) Extreme ultraviolet spectroheliograph ATM experiment S082A. *ao* 16:870–878. <https://doi.org/10.1364/AO.16.000870>
- Ugarte-Urra I, Young PR, Brooks DH, et al (2023) The Case for Solar Full-disk Spectral Diagnostics: Chromosphere to Corona. *Frontiers in Astronomy and Space Sciences* 9:427. <https://doi.org/10.3389/fspas.2022.1064192>
- Voronov DL, Gawlitza P, Cambie R, et al (2012) Conformal growth of Mo/Si multilayers on grating substrates using collimated ion beam sputtering. *Journal of Applied Physics* 111(9):093521–093521-9. <https://doi.org/10.1063/1.4710985>
- Wilhelm K, Curdt W, Marsch E, et al (1995) SUMER - Solar Ultraviolet Measurements of Emitted Radiation. *solphys* 162(1-2):189–231. <https://doi.org/10.1007/BF00733430>
- Windt DL (1998) IMD—Software for modeling the optical properties of multilayer films. *Computers in Physics* 12(4):360–370. <https://doi.org/10.1063/1.168689>
- Winebarger AR, Weber M, Bethge C, et al (2019) Unfolding Overlapped Slitless Imaging Spectrometer Data for Extended Sources. *apj* 882(1):12. <https://doi.org/10.3847/1538-4357/ab21db>, [arXiv:1811.08329](https://arxiv.org/abs/1811.08329) [astro-ph.SR]
- Xu Y, Tian H, Hou Z, et al (2022) Sun-as-a-star Spectroscopic Observations of the Line-of-sight Velocity of a Solar Eruption on 2021 October 28. *apj* 931(2):76. <https://doi.org/10.3847/1538-4357/ac69d5>, [arXiv:2204.11722](https://arxiv.org/abs/2204.11722) [astro-ph.SR]
- Yang Z, Tian H, Bai X, et al (2022) Can we detect coronal mass ejections through asymmetries of sun-as-a-star extreme-ultraviolet spectral line profiles? *The Astrophysical Journal Supplement Series* 260(2):36. <https://doi.org/10.3847/1538-4365/>

ac6607, URL <https://dx.doi.org/10.3847/1538-4365/ac6607>

Young PR (2021) Future Prospects for Solar EUV and Soft X-ray Solar Spectroscopy Missions. *Frontiers in Astronomy and Space Sciences* 8:50. <https://doi.org/10.3389/fspas.2021.662790>, [arXiv:2102.02943](https://arxiv.org/abs/2102.02943) [astro-ph.SR]

Young PR, Del Zanna G, Landi E, et al (2003) CHIANTI-An Atomic Database for Emission Lines. VI. Proton Rates and Other Improvements. *apjs* 144(1):135–152. <https://doi.org/10.1086/344365>, [arXiv:astro-ph/0209493](https://arxiv.org/abs/astro-ph/0209493) [astro-ph]